Centrum voor Wiskunde en Informatica

REPORT*RAPPORT*

MAS

Modelling, Analysis and Simulation

Modelling, Analysis and Simulation

A comparison of operator splitting and approximate matrix factorization for the shallow water equations in spherical geometry

D. Lanser

REPORT MAS-R0115 OCTOBER 31, 2001

CWI is the National Research Institute for Mathematics and Computer Science. It is sponsored by the Netherlands Organization for Scientific Research (NWO).
CWI is a founding member of ERCIM, the European Research Consortium for Informatics and Mathematics.

CWI's research has a theme-oriented structure and is grouped into four clusters. Listed below are the names of the clusters and in parentheses their acronyms.

Probability, Networks and Algorithms (PNA)

Software Engineering (SEN)

Modelling, Analysis and Simulation (MAS)

Information Systems (INS)

P.O. Box 94079, 1090 GB Amsterdam (NL)
Kruislaan 413, 1098 SJ Amsterdam (NL)
Telephone +31 20 592 9333
Telefax +31 20 592 4199

ISSN 1386-3703

A Comparison of Operator Splitting and Approximate Matrix Factorization for the Shallow Water Equations in Spherical Geometry

D. Lanser
CWI
P.O. Box 94079, 1090 GB Amsterdam, The Netherlands
email: debby.lanser@cwi.nl

ABSTRACT
The shallow water equations (SWEs) in spherical geometry provide a basic prototype for developing and testing numerical algorithms for solving the horizontal dynamics in global atmospheric circulation models. When solving the SWEs on a global fine uniform lat-lon grid, an explicit time integration method suffers from a severe stability restriction on the admissible step size. In a previous paper, we investigated an A-stable, linearly-implicit, third-order time integration method (Ros3), which we combined with approximate matrix factorization (AMF) to make it cost-effective. In this paper, we further explore this method and we compare it to a Strang-type operator splitting method. Our main focus is on the local error of the methods, their numerical dispersion relation and their accuracy and efficiency when applied to the well-known SWEs test set. The comparison shows that Ros3 with AMF accurately presents both low and mid frequency waves. Moreover, Ros3 with AMF makes a good candidate for the efficient solution of the SWEs on a global fine lat-lon grid. In contrast, Strang splitting is not advocated, in view of its inaccuracy in the polar area and the resulting inefficiency.

2000 Mathematics Subject Classification: Primary: 65M12, 86A10. Secondary: 65M06, 65M20, 76U05.
2000 ACM Computing Classification System: G.1.8.
Keywords and Phrases: Numerical time integration, shallow water equations in spherical geometry, operator splitting, approximate matrix factorization
Note: Work carried out under project MAS1.1 - Atmospheric Flow and Transport Problems.

1. Introduction

In current weather prediction and climate simulation, circulation models are used to simulate the dynamics of the atmosphere. A circulation model contains the primitive equations and a numerical solution method to solve them. Currently, there is a lot of interest in accurate and efficient numerical methods for global circulation models. Spectral methods, long considered ideal for numerical simulation on the sphere, proved less efficient on the high resolution grids demanded to progress atmospheric modeling. In [10, 11], we therefore investigated a new gridpoint method, which produced good results for the well established Shallow Water Equations (SWEs) testset [20]. This testset was developed to guide and stimulate the development of new numerical methods in circulation models and to provide a standard framework to assess them.

In [10], we discussed an Osher-type finite volume method for the spatial discretization of the SWEs on the sphere. Combined with a third-order upwind scheme for the constant state interpolation, this method is second-order accurate on uniform latitudinal-longitudinal (lat-lon) grids. In addition, we proposed an efficient time integration method in [11] for solving the resulting semi-discrete system. We applied a linearly implicit A-stable third-order Rosenbrock method (Ros3) to avoid the stability restriction associated with the well-known pole problem on uniform lat-lon grids and combined this method with approximate matrix factorization (AMF) to make it cost efficient. Ros3 with AMF produced good results for all testcases in the SWEs testset.

In this article, we further explore Ros3 with AMF and compare it to a Strang splitting method. Although both methods apply a splitting principle to simplify the solution process, their underlying techniques are very different. Strang splitting is an operator splitting technique, i.e., the original PDE problem is splitted additively in simpler PDEs which are solved separately. AMF on the other

hand, factorizes the linear systems to be solved in the linearly implicit Ros3 method. In this work, we investigate the local error of both techniques, in particular, in the polar area. Furthermore, we investigate their numerical dispersion relations to analyze their influence on the characteristic waves of the shallow water problem.

In meteorological practice, operator splitting techniques are considered unfit to solve the SWEs when they split the advection and Coriolis terms. Together these terms generate so called Rossby waves, which describe an important part of atmospheric dynamics. The separate treatment of the advection and Coriolis terms appears to jeopardize a correct representation of the Rossby waves and therefore appears to obstruct a correct representation of the atmospheric tendency to geostrophic balance. We will show that Ros3 with AMF solves the Rossby waves accurately.

The theoretical analysis of the local error and the numerical dispersion relations serves to demonstrate that Ros3 with AMF is particularly useful to efficiently integrate the SWEs in time on high resolution grids. In addition, the results are used to illustrate that a certain skepticism with respect to operator splitting methods is justified. The theoretical results will be confirmed by numerical experiments on the SWEs testset.

This paper is organized as follows. Section 2 describes the SWEs in spherical coordinates and gives a simplified formulation in a local Cartesian frame of reference. In Section 3, we consider the time integration methods, Ros3 with AMF and Strang splitting. Special attention is paid to accuracy and stability. Section 4 to Section 6 contain the actual comparisons between Ros3 with AMF and Strang splitting. Section 4 focuses on the local error of both methods when applied to the linearized SWEs in spherical coordinates. In Section 5, we analyze their numerical dispersion relations and demonstrate their influence on the characteristic waves associated with the original shallow water problem. In Section 6, we verify our theoretical results with numerical experiments. For that purpose, we concentrate on three test cases of the SWEs testset, i.e., Test Case 2, global steady-state non-linear zonal geostrophic flow, Test Case 5, zonal flow over an isolated mountain, and Test Case 6, the Rossby-Haurwitz wave. Finally, we formulate our conclusions in Section 7.

2. The Shallow Water Equations in spherical geometry

The Shallow Water Equations on the sphere describe a flow in a shallow homogeneous incompressible and inviscid fluid layer on a rotating sphere. Since they cover important aspects of the horizontal dynamical behavior of the atmosphere, these equations serve as a first prototype of a circulation model. More specifically, they regard the atmosphere as a thin layer in which the density is uniform and constant and in which viscous effects can be ignored. In this section, we briefly recall their formulation, see also [10, 20]. For a thorough derivation, we refer to [2, 7, 14, 18].

Let (λ, ϕ, t) denote the independent variables longitude, $\lambda \in [0, 2\pi)$, latitude, $\phi \in [-\pi/2, \pi/2]$, and time, $t \geq 0$. Let u be the velocity in longitudinal direction defined by $u = a/\cos(\phi)\ \mathrm{d}\lambda/\mathrm{d}t$, v the velocity in latitudinal direction defined by $v = a\ \mathrm{d}\phi/\mathrm{d}t$ and H the depth of the fluid layer. Let h denote the height of the free surface above the sphere at sea level, i.e., $h = H + h_s$, where h_s accounts for the orography of the earth and define $\underline{u}$ as the horizontal velocity field (u, v). Finally, let a denote the radius of the earth, g the gravitational constant and f the Coriolis parameter, $2\Omega \sin\phi$, with Ω the angular velocity of the earth. The shallow water equations on the sphere are then formulated as

$$\frac{\partial Hu}{\partial t} + \nabla \cdot (Hu\underline{u}) = (f + \frac{u}{a}\tan\phi)\, Hv - \frac{gH}{a\cos\phi}\frac{\partial h_s}{\partial \lambda} - \frac{g}{a\cos\phi}\frac{\partial (\frac{1}{2}H^2)}{\partial \lambda}, \tag{2.1}$$

$$\frac{\partial Hv}{\partial t} + \nabla \cdot (Hv\underline{u}) = -(f + \frac{u}{a}\tan\phi)\, Hu - \frac{gH}{a}\frac{\partial h_s}{\partial \phi} - \frac{g}{a}\frac{\partial (\frac{1}{2}H^2)}{\partial \phi}, \tag{2.2}$$

$$\frac{\partial H}{\partial t} + \nabla \cdot (H\underline{u}) = 0, \tag{2.3}$$

where the divergence operator is defined by

$$\nabla \cdot \underline{u} = \frac{1}{a\cos\phi}\left[\frac{\partial u}{\partial \lambda} + \frac{\partial (v\cos\phi)}{\partial \phi}\right]. \tag{2.4}$$

The above equations are given in flux-form, which directly originates from the corresponding conservation laws. The first and second equation describe conservation of momentum in longitudinal and latitudinal direction, respectively. The third equation is known as the continuity equation. The source terms on the right hand side are connected to the Coriolis force, the curvature terms, and the hydrostatic pressure gradient force.

2.1 The locally Cartesian form of the Shallow Water Equations

To facilitate the analysis of the numerical dispersion relations of our time integration methods, see Section 5, we also rely on a simpler version of the SWEs, viz. the SWEs in a locally Cartesian frame of reference. These equations are valid in a midlatitude synoptic system, which types of motion are common in dynamic meteorological practice. Based on midlatitude synoptic scale analysis, we are allowed to neglect the curvature terms in equations (2.1)–(2.3). In addition, we assume that the earth is an ideal sphere, i.e., $h_s = 0$. Using the flux form, the SWEs in a locally Cartesian frame of reference are then defined as

$$\frac{\partial Hu}{\partial t} + \frac{\partial Hu^2}{\partial x} + \frac{\partial Huv}{\partial y} + g\frac{\partial \frac{1}{2}H^2)}{\partial x} - fHv = 0, \tag{2.5}$$

$$\frac{\partial Hv}{\partial t} + \frac{\partial Huv}{\partial x} + \frac{\partial Hv^2}{\partial y} + g\frac{\partial \frac{1}{2}H^2)}{\partial y} + fHu = 0, \tag{2.6}$$

$$\frac{\partial H}{\partial t} + \frac{\partial Hu}{\partial x} + \frac{\partial Hv}{\partial y} = 0, \tag{2.7}$$

where the x- and y-coordinate are everywhere aligned with the local east- and northward direction, respectively. u and v denote the velocity components in these directions. Note that the absence of the curvature terms does not affect any analysis concerning the impact of splitting the Coriolis force from the advection terms in numerical time integration methods.

3. The time integration methods

In this section we discuss the third-order Rosenbrock method (Ros3) combined with approximate matrix factorization (AMF) and a Strang splitting method. These integration methods solve general non-linear ODE systems $\dot{\mathbf{w}} = \mathbf{F}(\mathbf{w})$. Note that any semi-discrete system of the SWEs fits into this framework, because the SWEs describe a pure initial value problem. These methods were also discussed in our earlier papers [11] and [12], respectively.

Both integration methods rely on a splitting principle, but on a different level in the solution process. Strang splitting is an operator splitting method, see [17]. It splits the different operators in the original PDE problem and solves them independently in successive substeps. Approximate matrix factorization simplifies the integration by factorizing the linear systems to be solved in the linearly implicit Ros3 method, such that these solves become less expensive.

Besides a general description of these methods, we will discuss their stability properties, which are of particular interest for meteorological applications. When calculating on a high resolution latitudinal-longitudinal grid, most time integration methods, read explicit methods, suffer from a severe restriction on the applicable time step. Since high resolution grids are the future trend, it is important to develop time integration methods which avoid such a limitation, see [19].

3.1 The third-order Rosenbrock method with approximate matrix factorization
We first concern ourselves with the third-order two-stage Rosenbrock method, see [3, 6, 11],

$$\begin{aligned} \mathbf{w}^{n+1} &= \mathbf{w}^n + \tfrac{5}{4}\mathbf{k}_1 + \tfrac{3}{4}\mathbf{k}_2, \\ S\mathbf{k}_1 &= \tau\,\mathbf{F}(\mathbf{w}^n), \\ S\mathbf{k}_2 &= \tau\,\mathbf{F}(\mathbf{w}^n + \tfrac{2}{3}\mathbf{k}_1) - \tfrac{4}{3}\mathbf{k}_1, \\ S &= (I - \gamma\tau J) \text{ with } \gamma = \tfrac{1}{2} + \tfrac{1}{6}\sqrt{3}, \end{aligned} \tag{3.1}$$

where $\tau = t_{n+1} - t_n$ denotes the step size, $\mathbf{w}^n$ denotes the numerical solution which approximates the exact solution $\mathbf{w}$ at time t_n, and $J = F'(\mathbf{w}^n)$ denotes the Jacobian matrix $d\mathbf{F}/d\mathbf{w}$ of $\mathbf{F}(\mathbf{w})$ at $\mathbf{w} = \mathbf{w}^n$. This method is called linearly implicit, since it requires the solution of two linear systems with the matrix $(I - \gamma\tau J)$. In this sense, the method is intermediate between explicit and implicit Runge-Kutta methods.

The Rosenbrock method is A-stable with stability function

$$R(z) = 1 + \frac{2z}{1-\gamma z} + \frac{\frac{1}{2}z^2 - z}{(1-\gamma z)^2},$$

see [6]. A-stability is attractive as it implies unconditional stability in the sense of Fourier-Von Neumann analysis [5, 18] for stable linear PDE problems.

A drawback of the Ros3 method (3.1) is that for multidimensional applications solving twice per time step a linear system with the matrix $I - \gamma\tau J$ is expensive. To reduce computational costs, while preserving A-stability and third-order accuracy, we therefore apply approximate matrix factorization. To demonstrate this technique, we rewrite the original ODE system as

$$\dot{\mathbf{w}} = \mathbf{F}(\mathbf{w}) = \mathbf{F}_\lambda(\mathbf{w}) + \mathbf{F}_\phi(\mathbf{w}), \tag{3.2}$$

where $\mathbf{F}_\lambda$ and $\mathbf{F}_\phi$ denote semi-discrete operators in longitudinal and latitudinal direction, respectively. In general, $\mathbf{F}$ also contains source terms, the distribution of which is not immediately evident from the definition of $\mathbf{F}_\lambda$ and $\mathbf{F}_\phi$. At this point we only assume that the source terms are distributed over $\mathbf{F}_\lambda$ and $\mathbf{F}_\phi$ in some appropriate manner. A detailed discussion on the distribution of the source terms is presented in Section 5.3.

The idea of approximate matrix factorization (AMF), see e.g. [1, 4, 9, 13], is to redefine S by

$$S = (I - \gamma\tau J_\lambda)\,(I - \gamma\tau J_\phi), \quad J_\lambda = F'_\lambda(\mathbf{w}^n), \quad J_\phi = F'_\phi(\mathbf{w}^n). \tag{3.3}$$

This significantly reduces the computational costs associated with the linear system solution. Instead of solving two huge two-dimensional linear systems per time step, we only have to solve four one-dimensional linear systems, each of which is uncoupled per grid line. While improving efficiency, Ros3 with AMF does not compromise the favorable properties of the original Ros3 method. First, Ros3 with AMF remains third-order accurate, see [11]. Second, Ros3 with AMF remains A-stable with stability function,

$$R(z_\lambda, z_\phi) = 1 + \frac{2z}{(1-\gamma z_\lambda)\,(1-\gamma z_\phi)} + \frac{\frac{1}{2}z^2 - z}{(1-\gamma z_\lambda)^2\,(1-\gamma z_\phi)^2},$$

where $z = z_\lambda + z_\phi$, see Theorem 3.1 in [11]. Theorem 3.1 implies that for matrices J_λ and J_ϕ which have a common complete system of eigenvectors, unconditional stability holds for stable linear problems in the sense of Fourier-Von Neumann analysis. Note that this is the case if these matrices commute. Although in general the matrices J_λ and J_ϕ do not commute, the theorem gives an indication for unconditional stability in practical applications.

3.2 The second-order Strang splitting method

Strang splitting belongs to the family of operator splitting methods. Operator splitting is based on the idea that most time-dependent ODE or PDE systems can be splitted additively in ODE or PDE systems which are simpler to solve. We can think for instance of the earlier subdivision of $\mathbf{F}$ in a longitudinal and a latitudinal part, respectively. In each time step of the operator splitting method the subprocesses are treated separately using a certain order of reappearance. We adopt the symmetrical order of reappearance proposed by Strang [17], for which he proved second-order consistency.

We demonstrate this form of symmetrical Strang splitting for system (3.2). Let the numerical solution $\mathbf{w}^n$ approximate $\mathbf{w}$ at time t_n and let $\tau = t_{n+1} - t_n$ denote the step size. Furthermore, let $\mathbf{w}_1(t)$ denote the solution of the subprocess $\dot{\mathbf{w}}_1 = \mathbf{F}_\lambda(\mathbf{w}_1)$ etc. Solving the substeps sequentially, one Strang splitting step from time t_n to t_{n+1} is given by

$$\dot{\mathbf{w}}_1 = \mathbf{F}_\lambda(\mathbf{w}_1), \quad \mathbf{w}_1(t_n) = \mathbf{w}^n, \qquad \text{for } t_n \le t \le t_{n+\frac{1}{2}}, \tag{3.4}$$

$$\dot{\mathbf{w}}_2 = \mathbf{F}_\phi(\mathbf{w}_2), \quad \mathbf{w}_2(t_n) = \mathbf{w}_1(t_n + \tfrac{\tau}{2}), \qquad \text{for } t_n \le t \le t_{n+1}, \tag{3.5}$$

$$\dot{\mathbf{w}}_3 = \mathbf{F}_\lambda(\mathbf{w}_3), \quad \mathbf{w}_3(t_n + \tfrac{\tau}{2}) = \mathbf{w}_2(t_n + \tau), \quad \text{for } t_{n+\frac{1}{2}} \le t \le t_{n+1}, \tag{3.6}$$

$$\Rightarrow \quad \mathbf{w}^{n+1} = \mathbf{w}_3(t_n + \tau). \tag{3.7}$$

This process is second order in time under the assumption that the subprocesses are solved exactly or numerically with an integration method of at least order two. The error introduced by the splitting is called the splitting error. In case of commuting operators, i.e., $F'_\lambda \mathbf{F}_\phi - F'_\phi \mathbf{F}_\lambda \equiv 0$, this splitting error is zero, see [12, 15, 16]. In practice, most systems do not commute, so we always have a splitting error.

4. The local error

In this section, we focus on the structure of the local error for both integration methods. Our interest is in these errors in the polar area. In actual applications, the local error of the Strang splitting method appears to increase significantly towards the poles as opposed to Ros3 with AMF.

We analyze the local error for the 'frozen' linearized system of equations derived from (2.1)–(2.4). Let us linearize around a constant state vector $\overline{\mathbf{q}} = (\overline{Hu}, \overline{Hv}, \overline{H})^T$, where the upper bar refers to 'frozen' variables. Substituting $\mathbf{q} = \overline{\mathbf{q}} + \mathbf{q}'$ in (2.1)–(2.4), the resulting linearized system reads

$$\mathbf{q}_t + A\,\mathbf{q}_\lambda + B\,\mathbf{q}_\phi = C_{\text{cur}}\,\mathbf{q} + C_{\text{cor}}\,\mathbf{q}, \tag{4.1}$$

with the matrices A and B,

$$A = \frac{1}{\tilde{a}} \begin{pmatrix} 2\overline{u} & 0 & -\overline{u}^2 + g\overline{H} \\ \overline{v} & \overline{u} & -\overline{u}\,\overline{v} \\ 1 & 0 & 0 \end{pmatrix}, \quad B = \frac{1}{a} \begin{pmatrix} \overline{v} & \overline{u} & -\overline{u}\,\overline{v} \\ 0 & 2\overline{v} & -\overline{v}^2 + g\overline{H} \\ 0 & 1 & 0 \end{pmatrix}, \quad \tilde{a} = a\cos\phi, \tag{4.2}$$

and the force matrices C_{cur} and C_{cor},

$$C_{\text{cur}} = \begin{pmatrix} \frac{2\tan\phi}{a}\,\overline{v} & \frac{2\tan\phi}{a}\,\overline{u} & -\frac{2\tan\phi}{a}\,\overline{u}\,\overline{v} \\ -C_{12} & C_{11} & \frac{\tan\phi}{a}\,(\overline{u}^2 - \overline{v}^2) \\ 0 & \frac{\tan\phi}{a} & 0 \end{pmatrix}, \quad C_{\text{cor}} = \begin{pmatrix} 0 & f & 0 \\ -f & 0 & 0 \\ 0 & 0 & 0 \end{pmatrix}, \tag{4.3}$$

where we omitted the apostrophes in equation (4.1) and assumed the earth to be ideal, i.e., $h_s = 0$. Next, we define a uniform lat-lon grid with cell-centered grid points (λ_i, ϕ_j),

$$\lambda_i = \left(i - \frac{1}{2}\right)\Delta\lambda, \qquad \Delta\lambda = \frac{2\pi}{\text{nL}}, \qquad i = 1, \ldots, \text{nL},$$

$$\phi_j = -\frac{\pi}{2} + \left(j - \frac{1}{2}\right)\Delta\phi, \quad \Delta\phi = \Delta\lambda = \frac{\pi}{\text{nP}}, \quad j = 1, \ldots, \text{nP},$$

and let the grid function $q_{i,j}(t)$ denote the semi-discrete approximation to the solution $\mathbf{q}(\lambda_i, \phi_j, t)$ of (4.1) on this grid. Spatially discretizating system (4.1) then yields the following ODE system,

$$\frac{\mathrm{d}\mathbf{q}_{i,j}}{\mathrm{d}t} = L\,\mathbf{q}_{i,j},\ L = L_A + L_B + C_{\mathrm{cur}} + C_{\mathrm{cor}}, \tag{4.4}$$

where $L_A = -A\,\mathrm{D}_\lambda$ and $L_B = -B\,\mathrm{D}_\phi$. The matrices A and B are evaluated in each grid cell. D_λ and D_ϕ are linear difference operators in longitudinal and latitudinal direction, respectively. For instance, for a second order central discretization, they read

$$\mathrm{D}_\lambda \mathbf{q}_{i,j} = \frac{\mathbf{q}_{i+1,j} - \mathbf{q}_{i-1,j}}{\Delta\lambda},$$
$$\mathrm{D}_\phi \mathbf{q}_{i,j} = \frac{\mathbf{q}_{i,j+1} - \mathbf{q}_{i,j-1}}{\Delta\phi}.$$

Let L_λ and L_ϕ denote the linear splitting operators,

$$L_\lambda\,\mathbf{q}_{i,j} = [L_A + C_{\mathrm{cur}_\lambda} + C_{\mathrm{cor}_\lambda}]\,\mathbf{q}_{i,j}, \tag{4.5}$$
$$L_\phi\,\mathbf{q}_{i,j} = \left[L_B + C_{\mathrm{cur}_\phi} + C_{\mathrm{cor}_\phi}\right]\mathbf{q}_{i,j}, \tag{4.6}$$

with $C_{\mathrm{cur}_\lambda} + C_{\mathrm{cur}_\phi} = C_{\mathrm{cur}}$ and $C_{\mathrm{cor}_\lambda} + C_{\mathrm{cor}_\phi} = C_{\mathrm{cor}}$. System (4.4) can then be written as

$$\frac{\mathrm{d}\mathbf{q}_{i,j}}{\mathrm{d}t} = L_\lambda\,\mathbf{q}_{i,j} + L_\phi\,\mathbf{q}_{i,j}. \tag{4.7}$$

The distribution of the source terms over L_λ and L_ϕ is partly fixed. The linearized curvature terms C_{cur_λ} and C_{cur_ϕ} read

$$C_{\mathrm{cur}_\lambda} = \begin{pmatrix} 0 & 0 & 0 \\ -\frac{2\tan\phi}{a}\,\overline{u} & 0 & \frac{\tan\phi}{a}\,\overline{u}^2 \\ 0 & 0 & 0 \end{pmatrix}, \quad C_{\mathrm{cur}_\phi} = \begin{pmatrix} \frac{2\tan\phi}{a}\,\overline{v} & \frac{2\tan\phi}{a}\,\overline{u} & -\frac{2\tan\phi}{a}\,\overline{u}\,\overline{v} \\ 0 & \frac{2\tan\phi}{a}\,\overline{v} & -\frac{\tan\phi}{a}\,\overline{v}^2 \\ 0 & \frac{\tan\phi}{a} & 0 \end{pmatrix}. \tag{4.8}$$

The first matrix, C_{cur_λ}, is exclusively connected to the curvature terms in the original SWEs system associated with a change in orientation of the unit vector in longitudinal direction, see [8]. Similarly, the second matrix, C_{cur_ϕ}, contains matrix entries related to the linearized curvature terms associated with a change in orientation of the unit vector in latitudinal direction. However, this matrix also contains part of the divergence operator. Of course, other splittings are possible, but only splitting (4.8) is natural. With respect to the Coriolis terms, no additional assumptions are made.

Observe that system (4.7) fits into the framework (3.2) with the additional advantage that $\mathbf{F}_\lambda(\mathbf{w})$ and $\mathbf{F}_\phi(\mathbf{w})$ are linear functions. Therefore, we can analyze the local Strang splitting and Ros3 with AMF error for the general linear ODE system,

$$\dot{\mathbf{w}} = \mathbf{F}(\mathbf{w}) = \mathbf{F}_\lambda(\mathbf{w}) + \mathbf{F}_\phi(\mathbf{w}) \text{ with } \mathbf{F}'_\lambda = \text{constant},\ \mathbf{F}'_\phi = \text{constant}. \tag{4.9}$$

Let $\mathbf{w}(t_n)$ denote the exact solution of system (4.9) at time t_n and let $\tilde{\mathbf{w}}^{n+1}$ denote the numerical solution after one time step with a particular time integration method from initial condition $\mathbf{w}^n = \mathbf{w}(t_n)$. The local error is then defined as

$$E_{\mathrm{loc}}^{n+1} = \left\|\mathbf{w}(t_{n+1}) - \tilde{\mathbf{w}}^{n+1}\right\|,$$

where $\|\cdot\|$ denotes a suitable norm, e.g. the L_∞- or L_2-norm. Assume that each of the substeps in the Strang splitting method is solved exactly in time. Omitting higher order terms, Taylor

expansion of $\mathbf{w}(t_{n+1})$ and $\tilde{\mathbf{w}}^{n+1}$ around the exact solution $\mathbf{w}(t_n)$ then yields

$$E^{n+1}_{\mathrm{loc}_{\mathrm{Strang}}} \approx \frac{1}{24} \parallel \mathbf{F}'_\lambda \mathbf{F}'_\lambda \mathbf{F}_\phi(\mathbf{w}(t_n)) - 2\,\mathbf{F}'_\lambda \mathbf{F}'_\phi (\mathbf{F}_\lambda(\mathbf{w}(t_n)) + \mathbf{F}_\phi(\mathbf{w}(t_n))) + \mathbf{F}'_\phi \mathbf{F}'_\lambda (\mathbf{F}_\lambda(\mathbf{w}(t_n)) + 4\,\mathbf{F}_\phi(\mathbf{w}(t_n))) - 2\,\mathbf{F}'_\phi \mathbf{F}'_\phi \mathbf{F}_\lambda(\mathbf{w}(t_n)) \parallel \tau^3. \tag{4.10}$$

Similarly, we obtain the following local error for Ros3 with AMF

$$E^{n+1}_{\mathrm{loc}_{\mathrm{Ros}}} \approx \parallel \left(\tfrac{1}{24}+\tfrac{1}{36}\sqrt{3}\right) \mathbf{F}'\mathbf{F}'\mathbf{F}'\mathbf{F}(\mathbf{w}(t_n)) + \left(\tfrac{1}{12}+\tfrac{1}{18}\sqrt{3}\right) \left(\mathbf{F}'_\lambda \mathbf{F}'_\phi \mathbf{F}' + \mathbf{F}'\mathbf{F}'_\lambda \mathbf{F}'_\phi\right) \mathbf{F}(\mathbf{w}(t_n)) \parallel \tau^4. \tag{4.11}$$

In the polar area, the linear splitting operators (4.5) and (4.6) are dominated by the curvature terms, i.e., $L_\lambda \sim C_{\mathrm{cur}_\lambda}$ and $L_\phi \sim C_{\mathrm{cur}_\phi}$. The largest matrix entries of C_{cur_λ} and C_{cur_ϕ} behave as $\overline{u}^2/(a\cos\phi)$ or $\overline{u}/(a\cos\phi)$, respectively, which rapidly increases towards the poles. We here assume that $\overline{u}$ and $\overline{v}$ behave similarly. Consequently, the largest entries of $\mathbf{F}'_\lambda$ and $\mathbf{F}'_\phi$ behave as $\overline{u}/(a\cos\phi)$ or $\overline{u}^2/(a\cos\phi)$ in the polar area. Through (4.10) and (4.11), we then find

$$E^{n+1}_{\mathrm{loc}_{\mathrm{Strang}}} \sim \left(\overline{u}\,(\tau\,\overline{u}/(a\cos|\phi|))^3\right), \text{ and } E^{n+1}_{\mathrm{loc}_{\mathrm{Ros}}} \sim \left(\overline{u}\,(\tau\,\overline{u}/(a\cos|\phi|))^4\right). \tag{4.12}$$

Note that these estimates are based on a Taylor expansion and the ommittance of higher order terms, which is only valid, when the quotient $\tau\,\overline{u}/(a\cos\phi_{\mathrm{nP}})$ is sufficiently small.

For realistic values of τ, $\overline{u}$, and grid resolution $\Delta\phi$, the expressions in (4.12) demonstrate that the local Strang splitting error becomes much larger in the polar area than the local Ros3 with AMF error. This is exemplified in Figure 1, where we assume a typical fine grid resolution, i.e., $\Delta\lambda = \Delta\phi = \pi/\mathrm{nP}$ with $\mathrm{nP} = \frac{1}{2}\,\mathrm{nL} = 180$, $\overline{u} = 10\,\mathrm{m/s}$, and a step size $\tau = 300\,\mathrm{s}$ ($\tau \ll a\cos\phi_{\mathrm{nP}}$). In this figure, the quotients from equations (4.12) are plotted over a latitudinal range $\phi \in [\pi/2 - 9\,\pi/(2*\mathrm{nP}),\ \pi/2 - \pi/(2*\mathrm{nP})]$, viz. the last five latitudinal grid points next to north pole. For Strang splitting, the local error increases rapidly in a band of three grid cells away from the pole. The increase of the local error of Ros3 with AMF on the other hand, is minor, and this error is significantly smaller as opposed to Strang splitting.

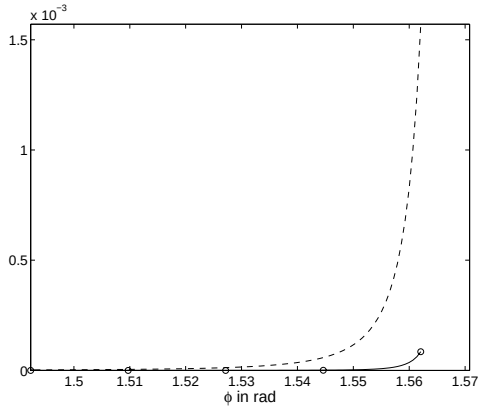

Figure 1: The quotient $\overline{u}\,(\tau\overline{u}/\,(a\cos\phi))^3$ for Strang splitting (*dashed*) and the quotient $\overline{u}\,(\tau\overline{u}/\,(a\cos\phi))^4$ for Ros3 with AMF (*solid*) over a latitudinal range $\phi \in [\pi/2 - 9\,\pi/(2*\mathrm{nP}),\ \pi/2 - \pi/(2*\mathrm{nP})]$, ($\mathrm{nP} = 180$, $\tau = 300\,\mathrm{s}$).

5. The dispersion relations

In meteorological practice, splitting methods are approached with a certain skepticism. It is considered unwise to split the process associated with advection waves from the Coriolis terms.

Together, these processes generate so called Rossby waves, which describe an important part of atmospheric dynamics. Treating these processes separately appears to jeopardize a correct representation of these waves and, therefore, appears to obstruct a correct representation of the atmospheric tendency to geostrophic balance. To investigate this matter, we focus on the dispersion relations of the time integration methods and compare them to the dispersion relation of the original problem. This analysis will show how the time integration method affects the amplitude and propagation velocity of the waves which build up the original solution.

5.1 The exact dispersion relation

Since, in this section, we are primarily interested in the effects of different splittings of the advection term from the Coriolis term, it is sufficient to consider the SWEs in a local Cartesian frame of reference, (2.5)–(2.7). To derive the exact dispersion relation, we first linearize system (2.5)–(2.7) around a constant state vector $\bar{\mathbf{q}} = (\bar{U}, \bar{V}, \bar{H})^T$, where the upper bar refers to frozen variables. We substitute $u = \bar{U} + u'$, $v = \bar{V} + v'$ and $H = \bar{H} + h'$ in the equations, which gives

$$\frac{\partial u}{\partial t} + U\frac{\partial u}{\partial x} + V\frac{\partial u}{\partial y} + g\frac{\partial h}{\partial x} - fv = 0, \tag{5.1}$$

$$\frac{\partial v}{\partial t} + U\frac{\partial v}{\partial x} + V\frac{\partial v}{\partial y} + g\frac{\partial h}{\partial y} + fu = 0, \tag{5.2}$$

$$\frac{\partial h}{\partial t} + U\frac{\partial h}{\partial x} + V\frac{\partial h}{\partial y} + H\frac{\partial u}{\partial x} + H\frac{\partial v}{\partial y} = 0, \tag{5.3}$$

where we omitted the upper bars and apostrophes for clarity. We then assume the harmonic wave solution,

$$\mathbf{q} = (u, v, h)^T = \breve{\mathbf{q}}(t)\, e^{i\,(\mathbf{k}\cdot\mathbf{x})} \text{ with } \breve{\mathbf{q}}(t) = \hat{\mathbf{q}}\, e^{-i\omega t}, \tag{5.4}$$

where $\mathbf{k} = (k_1, k_2)^T \in \mathbb{R}$, $\omega \in \mathbb{C}$ and $\hat{\mathbf{q}} =$ constant denote the wave number, the frequency and the amplitude of the wave, respectively. The frequency ω can be broken down into an imaginary part $\mathrm{Im}(\omega)$, which corresponds to damping or amplification, and a real part $\mathrm{Re}(\omega)$, which corresponds to propagation. With propagation, we associate the phase velocity c_p defined by

$$c_p = \frac{\mathrm{Re}(\omega)}{|\mathbf{k}|},$$

which says that any particular phase surface, i.e., a surface with a constant phase $\theta = \mathbf{k}\cdot\mathbf{x} - \mathrm{Re}(\omega)t$, moves with normal velocity c_p in the direction of $\mathbf{k}$. When the phase velocity depends on the wavenumber $\mathbf{k}$, the wave is called dispersive.

Substituting the harmonic wave solution into equations (5.1)-(5.3) yields

$$\begin{pmatrix} -i\omega + Uik_1 + Vik_2 & -f & gik_1 \\ f & -i\omega + Uik_1 + Vik_2 & gik_2 \\ Hik_1 & Hik_2 & -i\omega + Uik_1 + Vik_2 \end{pmatrix} \hat{\mathbf{q}} = \mathbf{0}. \tag{5.5}$$

A non-trivial harmonic wave solution of (5.1)-(5.3) exists when system (5.5) is singular. In that case, the determinant of the matrix should be zero, i.e.,

$$\det = \tilde{\omega}^3 + \tilde{\omega}\left(f^2 + gH\left(k_1^2 + k_2^2\right)\right) = 0 \tag{5.6}$$

with $\tilde{\omega} = -i\omega + Uik_1 + Vik_2$. Equation (5.6) relates the frequency ω to the wavenumber $\mathbf{k} = (k_1, k_2)^T$. This relation is called the dispersion relation. The dispersion relation (5.6) allows three different harmonic wave solutions with frequencies,

$$\omega_{\mathrm{ex}_j}(k_1, k_2) = \begin{cases} Uk_1 + Vk_2, & \text{for} \quad j = 1, \\ Uk_1 + Vk_2 - \sqrt{f^2 + gH\,(k_1^2 + k_2^2)}, & \text{for} \quad j = 2, \\ Uk_1 + Vk_2 + \sqrt{f^2 + gH\,(k_1^2 + k_2^2)}, & \text{for} \quad j = 3, \end{cases} \tag{5.7}$$

and corresponding amplitudes,

$$\hat{\mathbf{q}}_1 = \begin{pmatrix} -gk_2 \\ gk_1 \\ -if \end{pmatrix}, \qquad \hat{\mathbf{q}}_{2,3} = \begin{pmatrix} igk_2 f \mp gk_1\sqrt{f^2+gH\left(k_1^2+k_2^2\right)} \\ -igk_1 f \mp gk_2\sqrt{f^2+gH\left(k_1^2+k_2^2\right)} \\ gH \end{pmatrix}. \tag{5.8}$$

The first family of waves are known as the vorticity or advection waves, which are slow waves. The second and the third family of waves are called Poincaré waves, which imply pure gravity waves when $f^2 \ll gH|\mathbf{k}|^2$. These waves are considered to be fast. Note that none of these waves involves damping.

5.2 The numerical dispersion relations

In this section we derive the numerical dispersion relations of our time integration methods. The numerical dispersion relation is obtained in a similar manner as for the exact problem, i.e., by assuming a harmonic wave solution for the numerical scheme associated with the time integration method. The resulting frequencies differ from the original ones in both the imaginary and real part. The first leads to a wave with a different amplitude, which is called dissipation or accumulation. The second leads to a wave with a different propagation or phase velocity, which is called dispersion.

The Rosenbrock method combined with approximate matrix factorization We first focus on the numerical dispersion relation associated with the third-order Rosenbrock method combined with approximate matrix factorization. Normally, a numerical dispersion relation is discussed in connection to a difference scheme, which is the result of a certain discretization in space and integration in time [18]. Below, we analyze the numerical dispersion relation associated with the time integration method for the continuous form of the linearized SWEs.

We write the linearized equations (5.1)-(5.3) in matrix form,

$$\frac{\partial \mathbf{q}}{\partial t} = -\begin{pmatrix} U & 0 & g \\ 0 & U & 0 \\ H & 0 & U \end{pmatrix}\frac{\partial \mathbf{q}}{\partial x} + \begin{pmatrix} fv \\ 0 \\ 0 \end{pmatrix} - \begin{pmatrix} V & 0 & 0 \\ 0 & V & g \\ 0 & H & V \end{pmatrix}\frac{\partial \mathbf{q}}{\partial y} + \begin{pmatrix} 0 \\ -fu \\ 0 \end{pmatrix}. \tag{5.9}$$

Substitution of (5.4) into equation (5.9) yields the following ODE system for the Fourier transform $\breve{\mathbf{q}}(t)$,

$$\begin{aligned} \frac{\mathrm{d}\breve{\mathbf{q}}}{\mathrm{d}t} \quad = \quad & -i\,k_1 \begin{pmatrix} U & 0 & g \\ 0 & U & 0 \\ H & 0 & U \end{pmatrix}\breve{\mathbf{q}} \quad + \begin{pmatrix} 0 & f & 0 \\ 0 & 0 & 0 \\ 0 & 0 & 0 \end{pmatrix}\breve{\mathbf{q}} + \\ & -i\,k_2 \begin{pmatrix} V & 0 & 0 \\ 0 & V & g \\ 0 & H & V \end{pmatrix}\breve{\mathbf{q}} \quad + \begin{pmatrix} 0 & 0 & 0 \\ -f & 0 & 0 \\ 0 & 0 & 0 \end{pmatrix}\breve{\mathbf{q}}. \end{aligned} \tag{5.10}$$

Next, we apply Ros3 with AMF to system (5.10), where we divide the right-hand side of (5.10) into a part depending on the wavenumber k_1 and a part depending on the wavenumber k_2, i.e.,

$$\frac{\mathrm{d}\breve{\mathbf{q}}}{\mathrm{d}t} = A(k_1)\,\breve{\mathbf{q}} + B(k_2)\,\breve{\mathbf{q}}. \tag{5.11}$$

This distribution corresponds to a dimensional splitting similar to (3.2). Note that with the specification of $A(k_1)$ and $B(k_2)$ the distribution of the Coriolis terms over these matrices is not yet fixed. At this point, we assume that $A(k_1)$ contains the first Coriolis matrix of equation (5.10) and $B(k_2)$ contains the second. In Section 5.3, other distributions will be considered.

The application of Ros3 with AMF to (5.10) yields

$$\breve{\mathbf{q}}^{n+1} = R(\tau, A(k_1), B(k_2))\,\breve{\mathbf{q}}^n, \tag{5.12}$$

where $\breve{\mathbf{q}}^n$ denotes the approximation of the Fourier transform $\breve{\mathbf{q}}(t)$ at time $t = t_n$ and the amplification factor $R(\tau, A(k_1), B(k_2))$ is defined by the stability function,

$$R_{\rm ros}(\tau, A, B) = I + 2\,\tau S^{-1}\,(A+B) + \tau S^{-1}\left(\frac{1}{2}\tau\,(A+B) - I\right) S^{-1}\,(A+B)$$

with the matrix $S = (I - \gamma\tau A)\,(I - \gamma\tau B)$. For a further discussion on this stability function, we refer to our earlier paper [11].

To derive the numerical dispersion relation, we then substitute the numerical harmonic wave solution,

$$\breve{\mathbf{q}}^n = \hat{\mathbf{q}}\, e^{-i\,\omega_{\rm ros} t_n}, \tag{5.13}$$

into (5.12) to obtain

$$M_{\rm ros}\,\hat{\mathbf{q}} = e^{-i\,\omega_{\rm ros}\tau}\,\hat{\mathbf{q}} \text{ with } M_{\rm ros} = R_{\rm ros}(\tau, A(k_1), B(k_2)).$$

This gives the following numerical dispersion relation,

$$\omega_{{\rm ros}_j} = \frac{\ln\left(\lambda_{M_{{\rm ros}_j}}\right)}{\tau}\, i, \tag{5.14}$$

where $\lambda_{M_{{\rm ros}_j}}$ denotes the j-th eigenvalue of the matrix $M_{\rm ros}$. Note that these eigenvalues can be complex, allowing both dispersion and dissipation or accumulation. A thorough analysis of the frequencies given by (5.14) will show how the corresponding waves relate to the waves of the original problem, see Section 5.3.

The Strang splitting method Next, we derive the numerical dispersion relation associated with the Strang splitting method. For its derivation, we adopt the same approach as above. So, we commence from system (5.11) to which we apply the Strang splitting method. In this case, the amplification factor $R(\tau, A(k_1), B(k_2))$ is defined by

$$R_{\rm str}(\tau, A, B) = \exp\left(A\frac{\tau}{2}\right) \exp\left(B\tau\right) \exp\left(A\frac{\tau}{2}\right).$$

Postulating the harmonic wave solution (5.13) for the Fourier transform $\breve{\mathbf{q}}(t)$ and following the same reasoning as above, we arrive at the following dispersion relation,

$$\omega_{{\rm str}_j} = \frac{\ln\left(\lambda_{M_{{\rm str}_j}}\right)}{\tau}\, i, \tag{5.15}$$

where $\lambda_{M_{{\rm str}_j}}$ denotes the j-th eigenvalue of the matrix $M_{\rm str} = R_{\rm str}(\tau, A(k_1), B(k_2))$.

5.3 An evaluation of the dispersion relations

In this section, we compare the exact and numerical dispersion relations (5.7), (5.14) and (5.15) to examine how well the numerical methods represent the characteristic waves of the original problem. The numerical method can damp or amplify these waves and change their phase velocity. Furthermore, the relations (5.14) and (5.15) can be used to investigate the effects of specific splittings of the advection from the Coriolis terms. The question is whether these splittings significantly influence the accuracy and/or stability of the resulting numerical method. We can easily redo the analysis of Section 5.2 to provide the correct numerical dispersion relations for a particular redistribution of the forces over the subprocesses in longitudinal and latitudinal direction.

In order to analyze the dispersion relations, we choose a typical setting of the parameters U, V, H, g and f. Since our original system (2.5)–(2.7) is based on midlatitude synoptic scale analysis, we apply synoptic scale values for these quantities, i.e., $U = V = 10\,\mathrm{m/s}$, $H = 10^4\,\mathrm{m}$ and $f = 2\Omega\sin(\pi/4)$, see [8]. The gravitational constant g is given as $g = 9.8\,\mathrm{m/s^2}$. Furthermore,

we have to specify the range of wave numbers in which we are interested. For convenience, we write the wave number vector $\mathbf{k} = (k_1, k_2)^T$ in terms of its length $|\mathbf{k}|$ and its direction β, so $\mathbf{k} = (k_1, k_2)^T = (|\mathbf{k}| \cos\beta, |\mathbf{k}| \sin\beta)^T$. We focus on wave number vectors with length $|\mathbf{k}| = 1$. These wave numbers include the family of advective waves with velocity $U\cos\beta + V\sin\beta$ and the two families of gravity waves with velocities $U\cos\beta + V\sin\beta \pm \sqrt{gH}$, where we used $f \ll \sqrt{gH}$. Finally, it is important to notice that we are calculating in a *local* Cartesian frame of reference. Observe that the distance Δx in the local frame of reference corresponds to a radial change of the longitude, $\Delta\lambda$. The corresponding distance on the sphere then reads $a\cos\phi\,\Delta\lambda$. Therefore, the stepsizes for mid-latitudinal motion in the local and global frame of reference, τ_{local} and τ_{global}, are related as

$$\tau_{\text{global}} = a\cos\pi/4\,\tau_{\text{local}} \approx 4.5 \cdot 10^6\,\tau_{\text{local}}.$$

We elaborate the numerical dispersion relations for increasing step sizes. The minimum and maximum value of the imaginary parts of the corresponding frequencies are given in Table 1. The minimum and maximum values are calculated over $\beta \in [0, 2\pi)$. Observe that the corresponding frequencies of the original waves have no imaginary part. The positive imaginary parts of the frequencies in Table 1 then illustrate that a Strang splitting method tends to amplify both advection and gravity waves.

In case of Ros3 with AMF no such behavior is found. Each wave is either damped by the numerical method or propagates with a constant amplitude. Note that this behavior characterizes the A-stability property. Furthermore, the results indicate that Ros3 with AMF damps the various waves more rigorously than Strang splitting. For all step sizes considered, the minimum values of the imaginary parts are smaller for Ros3 with AMF than for Strang splitting. In addition, for Ros3 with AMF, the fast gravity waves are more strongly damped than the slow advective wave. The damping of Strang splitting does not distinguish between slow and fast waves.

Finally, we focus on the imaginary parts of the frequencies for a common step size τ_{local}. Assume $\Delta x = 2\pi/360$, which corresponds to a fine uniform lat-lon grid with $\Delta\lambda = \Delta\phi = 2\pi/360$. For the given synoptic values, we can then derive a maximal step size τ_{local} prescribed by the CFL-restriction, when solving the SWEs by means of a third-order Runge-Kutta method, see [11],

$$\tau_{\text{local}} = \Delta x/(U + \sqrt{gH}) = 5.4 \cdot 10^{-5}\,\text{s}.$$

For this step size, both methods behave excellently. In particular, their influence on the important advective wave is negligible.

The relative errors in the phase velocities are displayed in Table 2. The relative error is defined as follows,

$$E_{c_p} = \frac{\text{Re}\,(\omega_{\text{num}}) - \text{Re}\,(\omega_{\text{exact}})}{\text{Re}\,(\omega_{\text{exact}})}.$$

Table 2 illustrates that the Strang splitting method does not affect the phase velocity of the advection wave. The gravity waves are changed by this method. Ros3 with AMF on the other hand, affects both phase velocities, although its effect on the gravity waves is minor compared to Strang splitting for $\tau_{\text{local}} \leq 10^{-3}\,\text{s}$. In meteorological practice, however, numerical methods are assessed by their capability to represent the advective wave. At large step sizes, $\tau_{\text{local}} = 10^{-3}$ and $\tau_{\text{local}} = 10^{-2}$, Ros3 with AMF poorly represents the advective wave phase velocities as opposed to Strang splitting. For common step sizes though, $\tau_{\text{local}} = 10^{-4}$ and $\tau_{\text{local}} = 10^{-5}$, Ros 3 with AMF has almost no effect on the advective wave phase velocity.

The effect of a specific splitting of the Coriolis and advection term on the stability properties is studied by a comparison of the imaginary parts of the frequencies for three different splittings.

τ_{local}	Strang		Ros3 with AMF	
	min	max	min	max
10^{-5}	$-0.78 \cdot 10^{-10}$	$0.67 \cdot 10^{-10}$	$-0.18 \cdot 10^{-8}$	0
	$-0.89 \cdot 10^{-10}$	$0.11 \cdot 10^{-9}$	$-0.98 \cdot 10^{-6}$	$-0.39 \cdot 10^{-6}$
	$-0.12 \cdot 10^{-9}$	$0.13 \cdot 10^{-9}$	$-0.98 \cdot 10^{-6}$	$-0.39 \cdot 10^{-6}$
10^{-4}	$-0.21 \cdot 10^{-8}$	$0.21 \cdot 10^{-8}$	$-0.18 \cdot 10^{-5}$	0
	$-0.11 \cdot 10^{-8}$	$0.11 \cdot 10^{-8}$	$-0.98 \cdot 10^{-3}$	$-0.39 \cdot 10^{-3}$
	$-0.11 \cdot 10^{-8}$	$0.11 \cdot 10^{-8}$	$-0.98 \cdot 10^{-3}$	$-0.39 \cdot 10^{-3}$
10^{-3}	$-0.21 \cdot 10^{-6}$	$0.21 \cdot 10^{-6}$	$-0.17 \cdot 10^{-2}$	$-0.90 \cdot 10^{-6}$
	$-0.11 \cdot 10^{-6}$	$0.11 \cdot 10^{-6}$	$-0.86 \cdot 10^{0}$	$-0.37 \cdot 10^{0}$
	$-0.11 \cdot 10^{-6}$	$0.11 \cdot 10^{-6}$	$-0.86 \cdot 10^{0}$	$-0.37 \cdot 10^{0}$
10^{-2}	$-0.26 \cdot 10^{-4}$	$0.26 \cdot 10^{-4}$	$-0.60 \cdot 10^{-1}$	$-0.12 \cdot 10^{-1}$
	$-0.13 \cdot 10^{-4}$	$0.13 \cdot 10^{-4}$	$-0.24 \cdot 10^{2}$	$-0.20 \cdot 10^{2}$
	$-0.13 \cdot 10^{-4}$	$0.13 \cdot 10^{-4}$	$-0.24 \cdot 10^{2}$	$-0.21 \cdot 10^{2}$

Table 1: Minimum and maximum values of the imaginary part of the frequencies for Strang splitting and Ros3 with AMF. The results are presented for splitting (5.16). The maxima are calculated for wave numbers $\mathbf{k} = (\sin(\beta), \cos(\beta))$, with $\beta \in [0, 2\pi)$. For each step size τ_{local}, the extrema associated with the numerical advection ($j = 1$) and the numerical gravity waves ($j = 2, 3$) are listed.

These are

$$A(k_1) = -ik_1 \begin{pmatrix} U & i\frac{f}{k_1} & g \\ 0 & U & 0 \\ H & 0 & U \end{pmatrix} \quad \text{and} \quad B(k_2) = -ik_2 \begin{pmatrix} V & 0 & 0 \\ -i\frac{f}{k_2} & V & g \\ 0 & H & V \end{pmatrix}, \tag{5.16}$$

$$A(k_1) = -ik_1 \begin{pmatrix} U & i\frac{f}{k_1} & g \\ -i\frac{f}{k_1} & U & 0 \\ H & 0 & U \end{pmatrix} \quad \text{and} \quad B(k_2) = -ik_2 \begin{pmatrix} V & 0 & 0 \\ 0 & V & g \\ 0 & H & V \end{pmatrix}, \tag{5.17}$$

$$A(k_1) = -ik_1 \begin{pmatrix} U & 0 & g \\ 0 & U & 0 \\ H & 0 & U \end{pmatrix} \quad \text{and} \quad B(k_2) = -ik_2 \begin{pmatrix} V & i\frac{f}{k_2} & 0 \\ -i\frac{f}{k_2} & V & g \\ 0 & H & V \end{pmatrix}. \tag{5.18}$$

The first splitting is already examined above. The second and third splitting involve no directional separation of the Coriolis terms. In Table 1, the minimum and maximum value of the imaginary parts of the numerical frequencies are given for the first splitting for Strang splitting and Ros3 with AMF, respectively. For Strang splitting, the minimal and maximal values for the second and third splitting (5.17)–(5.18) are close to zero, so only very small machine representation errors were visible. The difference of these values as opposed to the values for splitting (5.16) indicate that amplification or damping by Strang splitting indeed depends on the specific splitting. The method behaves significantly better in case of the second and third splitting, since they involve almost no damping or amplification. Ros3 with AMF, on the other hand, is almost indifferent to the details of the splitting. The entries of the minimum and maximum value for the second and third splitting were almost identical to the entries of splitting I.

6. Numerical experiments

In this section, we continue our comparison between Ros3 with AMF and Strang splitting by an assessment of these methods when applied to test cases of the well-established SWEs test set [20].

τ_{local}	max E_{c_p})	
	Strang	Ros3 with AMF
10^{-5}	0	$0.58 \cdot 10^{-13}$
	$0.11 \cdot 10^{-6}$	$0.11 \cdot 10^{-10}$
	$0.11 \cdot 10^{-6}$	$0.11 \cdot 10^{-10}$
10^{-4}	0	$3.09 \cdot 10^{-10}$
	$0.11 \cdot 10^{-4}$	$0.11 \cdot 10^{-6}$
	$0.11 \cdot 10^{-4}$	$0.11 \cdot 10^{-6}$
10^{-3}	0	$0.26 \cdot 10^{-4}$
	$0.11 \cdot 10^{-2}$	$0.10 \cdot 10^{-3}$
	$0.11 \cdot 10^{-2}$	$0.10 \cdot 10^{-3}$
10^{-2}	0	0.35
	0.13	0.33
	0.13	0.33

Table 2: Maximum value of the relative errors in the phase velocities for Strang splitting and Ros3 with AMF. The maxima are calculated for wave numbers $\mathbf{k} = (\sin(\beta), \cos(\beta))$, with $\beta \in [0, 2\pi)$. For each step size τ_{local}, the extrema associated with the numerical advection ($j = 1$) and the numerical gravity waves ($j = 2, 3$) are listed.

In addition, the numerical experiments serve to verify the theoretical results found in Section 4 and 5.

Both methods are used to integrate the system of ODEs resulting from spatially discretizing the full non-linear system of SWEs on the rotating sphere (2.1)–(2.4). Calculations are done on a uniform lat-lon grid. As spatial discretization scheme, we apply a finite volume method, viz. an Osher scheme combined with the ($\kappa = 1/3$)-scheme for the constant state interpolation, which proved to be well suited for solving the SWEs in spherical geometry, see [10]. Since the resulting ODE system is too difficult to be solved exactly, we have to specify the integration methods which are used to solve the substeps in the Strang splitting method. In our earlier paper, Ros3 with AMF proved far more efficient than the RK3 explicit method. Consequently, Strang splitting can only be cost effective when it is combined with an implicit time integration method. We therefore apply the Ros3 method (3.1). In addition, this method is third-order accurate, which ensures that the splitting error dominates the total error, and it is A-stable.

We concentrate on three different test cases from the well-known SWEs test set [20], viz. Test 2, global steady-state non-linear zonal geostrophic flow, Test 5, zonal flow over an isolated mountain, and Test 6, a Rossby-Haurwitz wave. All three test cases were discussed in earlier work [11]. Test 2 is used to provide an order estimate for the Strang splitting method similar to the one for Ros3 with AMF found in [11]. Test 5 and 6 are chosen, because they describe 'realistic' instationary flow patterns, and are therefore suitable to truly assess our time integration methods. In addition, they form an excellent framework to investigate the influence of the integration methods on various wave-like solutions. Test 5 involves high-amplitude gravity waves. Test 6 describes a slow Rossby-Haurwitz wave, whose flow pattern is very common in practical applications. A correct representation of this last wave is therefore of great importance.

The presentation of the numerical experiments is divided in two parts.

- First, we investigate the accuracy and efficiency of both methods for a specific splitting. As reference splitting, we use the splitting suggested in our previous paper. The results are used to identify the extent of the errors and their location on the sphere. The calculations are performed on a high resolution grid, viz. a uniform lat-lon grid with 180 grid points in latitudinal direction (nP = 180) and 360 grid points in longitudinal direction (nL = 360)($1^\circ \times 1^\circ$).

The step sizes of each method are determined by trial and error. For Strang splitting, they will be the maximal step sizes at which stability is obtained and accuracy is still acceptable. For Ros3 with AMF, the step sizes are chosen such that its results are equally accurate as these of Strang splitting.

- Second, we investigate the effects of various splittings on the accuracy and efficiency of both methods. Calculations are done on a uniform lat-lon grid of 90×180 grid points in case of Test 5 and on a uniform lat-lon grid of 144×288 grid points in case of Test 6. These grids are coarser than the previous to confine the error in the polar area, see Section 4. The step size is fixed for all splittings.

In both parts, the accuracy is expressed by the l_2- or l_∞-norm of the relative error of the depth of the fluid layer and the absolute errors of the velocity components in longitudinal- and latitudinal direction. In spherical geometry the discrete l_∞-norm and l_2-norms are defined as follows,

$$l_\infty(H) = \max_{i,j} \left| \frac{H_{i,j} - H(\lambda_i, \phi_j)}{H(\lambda_i, \phi_j)} \right|, \tag{6.1}$$

$$l_\infty(u) = \max_{i,j} | u_{i,j} - u(\lambda_i, \phi_j) |, \tag{6.2}$$

$$l_2(H) = \sqrt{\sum_{i,j} \left(H_{i,j} - H(\lambda_i, \phi_j)\right)^2 \cos\phi_j} \Bigg/ \sqrt{\sum_{i,j} \left(H(\lambda_i, \phi_j)\right)^2 \cos\phi_j}, \tag{6.3}$$

$$l_2(u) = \frac{\sqrt{\pi}}{\mathrm{nL}} \sqrt{\sum_{i,j} \left(u_{i,j} - u(\lambda_i, \phi_j)\right)^2 \cos\phi_j}, \tag{6.4}$$

where $H_{i,j}$ etc. denote the approximated solution H etc. at gridpoint (λ_i, ϕ_j) and $H(\lambda_i, \phi_j)$ etc. denote the reference solution H etc. at gridpoint (λ_i, ϕ_j), which is exact in case of Test 2 and given by a high resolution spectral method in case of Test 5 and Test 6. Note that $l_2(H)$ and $l_2(u)$ are the high-resolution finite volume equivalents of the continuous l_2-norm defined by Williamson et al in [20].

6.1 The three test cases from the SWEs test set

First, we summarize the three considered test cases from the SWE test set, viz. Test 2, Test 5, and Test 6. Test 2 represents a solid body rotation of which the height field and the velocity components in longitudinal and latitudinal direction are defined as follows

$$H = h_0 - \left(\frac{a\Omega u_0}{g} + \frac{u_0^2}{2g}\right) \left(-\cos\lambda\cos\phi\sin\alpha + \sin\phi\cos\alpha\right)^2, \tag{6.5}$$

$$u = u_0 \left(\cos\phi\cos\alpha + \sin\phi\cos\lambda\sin\alpha\right), \tag{6.6}$$

$$v = -u_0 \sin\lambda \sin\alpha, \tag{6.7}$$

with h_0 and u_0 given, $u_0 = 38.6\,\mathrm{m/s}$ and $gh_0 = 2.94 \cdot 10^4\,\mathrm{m^2/s^2}$. α denotes the angle between the axis of the solid body rotation and the polar axis of the spherical coordinate system. We consider flow over the poles, i.e., $\alpha = \pi/2$. Test 2 extends over a 5-days interval.

Test 5 represents a zonal flow which impinges on a mountain. The mountain height is prescribed by a cone,

$$h_s = h_{s_0} \left(1 - \frac{r}{R}\right), \tag{6.8}$$

where $h_{s_0} = 2000\,\mathrm{m}$, $R = \pi/9$, $r^2 = \min[R^2, (\lambda - \lambda_c)^2 + (\phi - \phi_c)^2]$, $\lambda_c = 3\pi/2$, and $\phi_c = \pi/6$. The initial zonal flow is given by a solid body rotation parallel to the equator. The initial height and velocity components result from equation (6.5)–(6.7) with $\alpha = 0$, $u_0 = 20\,\mathrm{m/s}$, and $h_0 = 5960\,\mathrm{m}$. The reference solution is determined by a high resolution spectral method. The simulated time period is 15 days.

Test 6 consists of a Rossby-Haurwitz wave with a simulation period of 14 days. The initial condition is provided in [20]. Meteorologists consider this test as standard, since similar flow patterns occur in practical applications. A reference solution over a fourteen days interval is provided by a high resolution spectral circulation model.

6.2 Experiments with the reference splitting

The reference splitting In this section, we specify the reference splitting for which we assess Strang splitting and Ros3 with AMF on a high-resolution grid. Similar to Section 4, this splitting is defined by

$$\frac{\partial \mathbf{q}}{\partial t} = \mathbf{f}_\lambda(\mathbf{q}) + \mathbf{f}_\phi(\mathbf{q}) \tag{6.9}$$

with

$$\mathbf{f}_\lambda(\mathbf{q}) = \frac{-1}{a\cos\phi}\frac{\partial}{\partial\lambda}\begin{pmatrix} Hu^2 + \frac{1}{2}gH^2 \\ Huv \\ Hu \end{pmatrix} + \begin{pmatrix} -\frac{gH}{a\cos\phi}\frac{\partial h_s}{\partial\lambda} + fHv \\ -\frac{Hu^2}{a}\tan\phi \\ 0 \end{pmatrix}, \tag{6.10}$$

$$\mathbf{f}_\phi(\mathbf{q}) = \frac{-1}{a\cos\phi}\frac{\partial}{\partial\phi}\begin{pmatrix} Huv\cos\phi \\ \left(Hv^2 + \frac{1}{2}gH^2\right)\cos\phi \\ Hv\cos\phi \end{pmatrix} + \begin{pmatrix} \frac{Huv}{a}\tan\phi \\ -\frac{gH}{a}\frac{\partial h_s}{\partial\phi} - fHu - \frac{\tan\phi}{2a}gH^2 \\ 0 \end{pmatrix}. \tag{6.11}$$

The curvature terms are distributed over $\mathbf{f}_\lambda$ and $\mathbf{f}_\phi$ respecting their association with a change of orientation of the corresponding unit vector. This distribution is natural. The Coriolis forces are assigned according to the direction of the momentum equations from which they originate. With a minor difference in the distribution of the curvature terms, this splitting was successfully applied in [11] for Ros3 with AMF.

An order estimate for Strang splitting First, we illustrate the order behavior of the Strang splitting method. Similar to the order estimate for Ros3 with AMF given in [11], calculations are done on a uniform lat-lon grid with resolution nL = 288 and nP = 144 for varying step sizes. We concentrate on Test 2. As order estimate, we use the l_∞-norm of the absolute error of H and u, defined as

$$\text{abs(var)}_\tau = \max_{i,j} \left|\text{var}^\tau_{i,j,t} - \text{var}^{\tau_{\text{ref}}}_{i,j,t}\right| \text{ with } \tau_{\text{ref}} = 80\,\text{s},$$

where $\text{var}^\tau_{i,j,t}$ yields the approximate value of a variable var in gridpoint (λ_i, ϕ_j) at time t calculated with step size τ. Figure 2 pictures these norms against the step size τ in a log-log plot. Note that we march to the steady-state of the semi-discrete problem. The figure illustrates that the order of the Strang splitting method is slightly higher than two in this case. By theory, second-order consistency is expected as is visualized by the slope of the solid line, which is two.

Results on Test 5 and Test 6 In this section, Ros3 with AMF and Strang splitting are applied to Test 5 and Test 6 of the SWEs test set. Our interest is in their accuracy and efficiency when used on a high resolution grid.

Calculations are done on a uniform lat-lon grid with nL = 360 and nP = 180. The step size is found by trial and error depending on the test case and the integration method. For Strang splitting we apply the following step sizes, $\tau = 216\,\text{s}$ in case of Test 5 and $\tau = 450\,\text{s}$ in case of Test 6. These step sizes are chosen such that the results are sufficiently accurate and the computation is stable. For Ros3 with AMF, the step sizes are chosen such that its results are equally accurate as these of Strang splitting. This yields $\tau = 900\,\text{s}$ in case of Test 5 and $\tau = 1200\,\text{s}$ in case of Test 6. Consequently, Ros3 with AMF is far more efficient than Strang splitting. Strang splitting involves three linear system solves and three flux evaluations per time step, where we accounted the flux

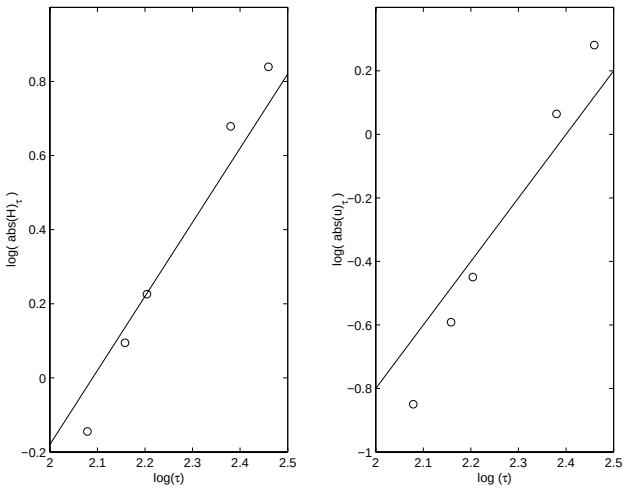

Figure 2: An order estimate for H and u: $\log(\text{abs}(H)_\tau)$ and $\log(\text{abs}(u)_\tau)$ versus $\log(\tau)$ for the Strang splitting method for Test 2 (markers). The solid lines illustrate formal second order accuracy.

evaluations of $\mathbf{F}_\lambda$ and $\mathbf{F}_\phi$ as two flux evaluations. Ros3 with AMF involves four linear system solves and four flux evaluations per time step. Therefore, if the step size for Ros3 with AMF is more than $4/3$ times as large as the step size of Strang splitting its workload is lower. For $\tau = 900\,\text{s}$ in case of Test 5 and $\tau = 1200\,\text{s}$ in case of Test 6, respectively, these ratios are 4.17 and 2.67, respectively. Finally, we comment that for Ros3 with AMF, results can be obtained for much larger step sizes. In contrast to Strang splitting, Ros3 with AMF does not suffer from a severe step size restriction. Note that, eventually, the step size for Ros3 with AMF is limited by accuracy. For very large step sizes, viz. several hours, Ros3 with AMF involves too much damping to correctly represent the solution, see Table 1 with $\tau_{\text{local}} \geq 10^{-3}\,\text{s}$.

Figure 3 represents the errors (6.1)–(6.4) for Test 5. The errors are sufficiently small, although the sudden increase of the $l_\infty(u)$ and $l_\infty(v)$ for Strang splitting is remarkable. This increase is caused by an interaction of the propagated spatial error, initially caused at the foot of the mountain, and the mountain itself. The spatial error is rotated over the sphere in approximately 10 days before it again impinges on the mountain. As a result, in case of Strang splitting, a sudden increase of the local error is observed. For Ros3 with AMF, this increase is not that apparent. The spatial errors involve high-frequency waves, which are strongly damped by Ros3 with AMF. Observe that this explanation agrees with the results from Section 5. The considered step sizes $\tau = 216\,\text{s}$ and $\tau = 900\,\text{s}$ in case of Strang splitting and Ros3 with AMF, respectively, correspond to $\tau_{\text{local}} = 4.8 \cdot 10^{-5}\,\text{s}$ and $\tau_{\text{local}} = 2.0 \cdot 10^{-4}\,\text{s}$, respectively. The fact that we do not observe a sudden increase of the $l_2(u)$ and $l_2(v)$-norm for Strang splitting, shows that the error increase is local in space.

Figure 4 represents the errors (6.1)–(6.4) for Strang splitting and Ros3 with AMF in case of Test 6. Again, similar accuracy is obtained, but for different step sizes in favor of Ros3 with AMF. The step size applied for Ros3 with AMF is again larger than $4/3$ times the stepsize applied for Strang splitting. The Rossby-Haurwitz represents a low frequency wave and is therefore of particular interest to meteorologists. According to Section 5, both methods do not significantly affect the advective wave phase velocity.

Finally, Figure 5 visualizes the relative error of H on the northern hemisphere projected onto the equatorial plane. This picture clearly demonstrates that the Strang splitting error is large in the polar region as opposed to Ros3 with AMF. This result confirms the results of Section 4, where we found that on current high resolution grids Strang splitting suffers more strongly from the pole singularity in the spherical SWEs, observable by large local errors in the polar region.

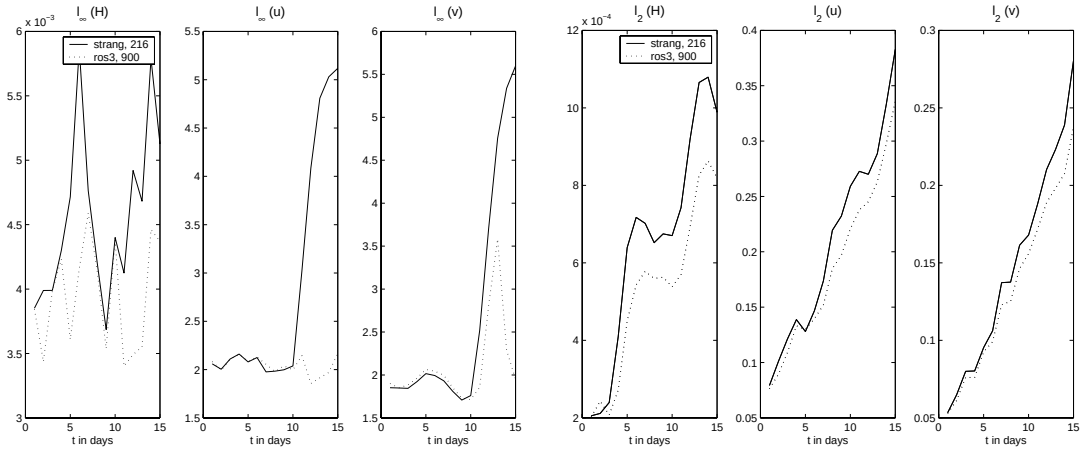

(a) l_∞-norm (b) l_2-norm

Figure 3: The l_∞-norm (fig(a)) and l_2-norm (fig(b)) of the relative error in H (first column), and absolute errors in u and v (second and third column) for Test 5 for Strang splitting (solid) and Ros3 with AMF (dotted) in case of the reference splitting.

6.3 Experiments with several other splittings

In this section, we consider several splittings of the SWEs in spherical geometry. The splittings differ in their distribution of the Coriolis forces over the flux functions $\mathbf{f}_\lambda$ and $\mathbf{f}_\phi$. Since the advection- and curvature terms are strongly connected to a specific direction, their distribution is fixed. So, we have

$$\mathbf{f}_\lambda(\mathbf{q}) = -\frac{1}{a\cos\phi}\frac{\partial}{\partial\lambda}\begin{pmatrix} Hu^2+\frac{1}{2}gH^2 \\ Huv \\ Hu \end{pmatrix} + \begin{pmatrix} -\frac{gH}{a\cos\phi}\frac{\partial h_s}{\partial\lambda} \\ -\frac{Hu^2}{a}\tan\phi \\ 0 \end{pmatrix} + \mathbf{f}_{\lambda_{\mathrm{Cor}}}(\mathbf{q}), \tag{6.12}$$

$$\mathbf{f}_\phi(\mathbf{q}) = -\frac{1}{a\cos\phi}\frac{\partial}{\partial\phi}\begin{pmatrix} Huv\cos\phi \\ \left(Hv^2+\frac{1}{2}gH^2\right)\cos\phi \\ Hv\cos\phi \end{pmatrix} + \begin{pmatrix} \frac{\frac{Huv}{a}\tan\phi}{} \\ -\frac{gH}{a}\frac{\partial h_s}{\partial\phi} - \frac{\tan\phi}{2a}gH^2 \\ 0 \end{pmatrix} + \mathbf{f}_{\phi_{\mathrm{Cor}}}(\mathbf{q}), \tag{6.13}$$

where $\mathbf{f}_{\lambda_{\mathrm{Cor}}}(\mathbf{q}) + \mathbf{f}_{\phi_{\mathrm{Cor}}}(\mathbf{q}) = (fHv, -fHu, 0)^T$. The different splittings are

$\mathbf{f}_{\lambda_{\mathrm{Cor}}}(\mathbf{q}) = (fHv, -fHu, 0)^T$,	$\mathbf{f}_{\phi_{\mathrm{Cor}}}(\mathbf{q}) = (0,0,0)^T$,	(f12f)
$\mathbf{f}_{\lambda_{\mathrm{Cor}}}(\mathbf{q}) = (0,0,0)^T$,	$\mathbf{f}_{\phi_{\mathrm{Cor}}}(\mathbf{q}) = (fHv, -fHu, 0)^T$,	(ff12)
$\mathbf{f}_{\lambda_{\mathrm{Cor}}}(\mathbf{q}) = (fHv, 0, 0)^T$,	$\mathbf{f}_{\phi_{\mathrm{Cor}}}(\mathbf{q}) = (0, -fHu, 0)^T$,	(f1f2)
$\mathbf{f}_{\lambda_{\mathrm{Cor}}}(\mathbf{q}) = (0, -fHu, 0)^T$,	$\mathbf{f}_{\phi_{\mathrm{Cor}}}(\mathbf{q}) = (fHv, 0, 0)^T$,	(f2f1)
$\mathbf{f}_{\lambda_{\mathrm{Cor}}}(\mathbf{q}) = \frac{1}{2}(fHv, -fHu, 0)^T$,	$\mathbf{f}_{\phi_{\mathrm{Cor}}}(\mathbf{q}) = \frac{1}{2}(fHv, -fHu, 0)^T$,	(fhalf)

where the first two splittings involve the complete assignment of the Coriolis forces to one direction. The third splitting is the reference splitting investigated in Section 6.2. Splitting four and five, (f2f1) and (fhalf), are artificial. Note that the first three splittings were considered before in Section 5.3 for the linearized local Cartesian SWEs.

We focus on Test 5 and Test 6 of the SWEs test set. Calculations are done on a 90×180 uniform lat-lon grid over a fifteen days time period for Test 5, and on 144×288 uniform lat-lon grid over a

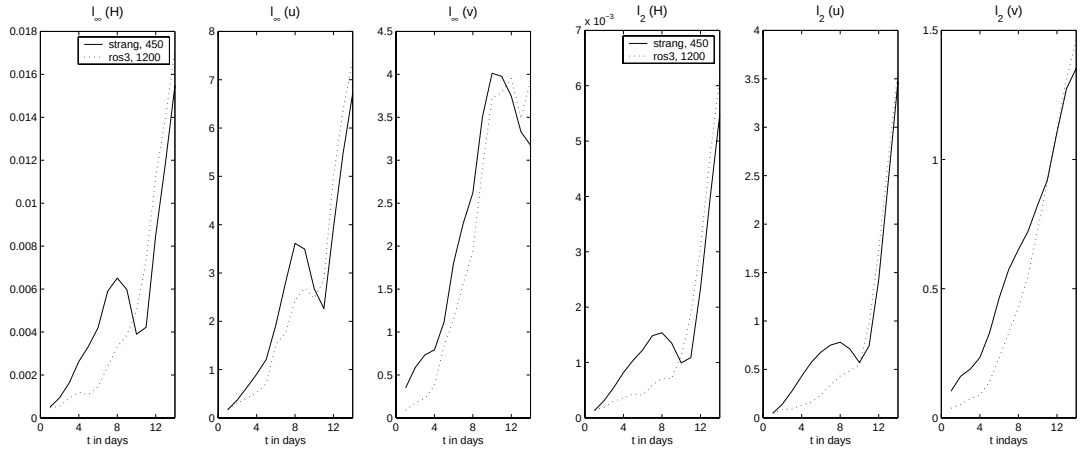

(a) l_∞-norm (b) l_2-norm

Figure 4: The l_∞-norm (fig(a)) and l_2-norm (fig(b)) of the relative error in H (first column), and absolute errors in u and v (second and third column) for Test 6 for Strang splitting (solid) and Ros3 with AMF (dotted) in case of the reference splitting.

fourteen days time period for Test 6, respectively. For Test 5, the Strang splitting method uses a fixed step size $\tau = 900\,\mathrm{s}$ for all splittings, Ros3 with AMF uses a step size $\tau = 1800\,\mathrm{s}$. The results of Test 6 are computed with a step size $\tau = 150\,\mathrm{s}$ for Strang splitting and $\tau = 450\,\mathrm{s}$ for Ros3 with AMF. The step sizes are chosen such that the results satisfy a given accuracy requirement for the reference splitting.

Since we are mainly interested in the qualitative difference between the results for the various splittings and in the impact of these splittings on the two integration methods, we introduce the following monitor,

$$\mathrm{reldif}\left(t, E, H_{(\mathrm{sp})}(t)\right) = \frac{E\left(H_{(\mathrm{sp})}(t)\right) - E\left(H_{(\mathrm{refsp})}(t)\right)}{E\left(H_{(\mathrm{refsp})}(t)\right)},$$

where $E(H)$ denotes the l_∞- or l_2-norm defined in (6.1) and (6.3), t denotes the time at which the solution $H_{(\mathrm{sp})}$ is approximated and (refsp) denotes the reference splitting (f1f2). Similar expressions can be derived for the longitudinal and latitudinal velocity components.

Figure 6–7 represent the relative differences, $\mathrm{reldif}(t, l_2, H)$, $\mathrm{reldif}(t, l_2, u)$, and $\mathrm{reldif}(t, l_2, v)$ for the several splittings when applied to Test 5 and Test 6. These figures demonstrate that it is difficult to identify a best splitting, because such a splitting depends on the specific test case. For instance, for Strang splitting, the reference splitting (f1f2) is not a good choice in case of Test 5. After 15-days, the l_2-norms of the relative error in H, and absolute errors in u and v are smaller for almost all other splittings, viz. $\mathrm{reldif}(t, l_2, H) < 0$ etc., see Figure 6(a). Splitting (f2f1) appears better suited. For Test 6, on the other hand, the reference splitting is less accurate over the first seven days, but performs better than the other splittings on the seven days remaining, see Figure 7(a).

Compared to Ros3 with AMF, Strang splitting is more sensitive to the chosen splitting. For this method, the relative differences vary over a range of $[-0.16, 0.10]$ in case of Test 5 and over a range of $[-0.18, 0.11]$ in case of Test 6, see Figure 6(a) and 7(a). For Ros3 with AMF, on the other hand, these differences vary over a range of $[-0.003, 0.03]$ in case of Test 5 and over a range of $\left[-2.5 \cdot 10^{-3}, 3.6 \cdot 10^{-3}\right]$ in case of Test 6, see Figure 6(b) and Figure 7(b), respectively. Ros3 with AMF is almost indifferent to the applied splitting, which agrees with our results in Section 5.3. For Ros3 with AMF the reference splitting is sufficiently accurate for both test cases, although

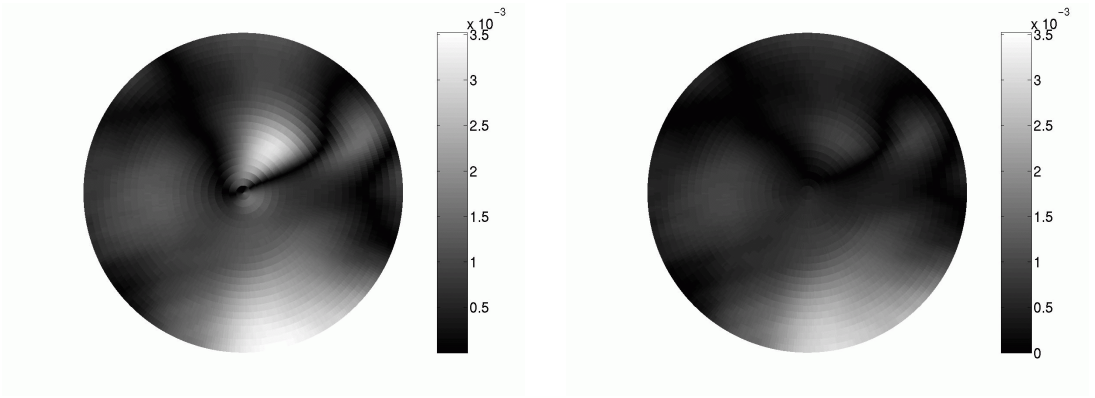

(a) Strang splitting ($\tau = 216$ s) (b) Ros3 with AMF ($\tau = 900$ s)

Figure 5: Polar view of the relative error in H for Test 5 for Strang splitting (fig(a)) and Ros3 with AMF (fig(b)), in case of the reference splitting. $\phi \in [\frac{7}{8}\pi, \frac{1}{2}\pi]$

splitting (f2f1) is slightly better.

7. Conclusion

When solving the semi-discrete SWEs on a global uniform lat-lon grid, an explicit time integration method suffers from a severe restriction on the step size (the pole problem). This problem can be avoided by the application of an implicit time integration method. In [11], we therefore investigated an A-stable linearly implicit 3rd-order time integration method, which we combined with approximate matrix factorization to make it cost effective, viz., Ros3 with AMF.

In this article, we further explored this method and compared it to a Strang-type splitting method. First, we focused on the local error of both methods for the linearized SWEs in spherical geometry. Strang splitting is showed to suffer from a large local error in the polar area as opposed to Ros3 with AMF. Second, we investigated the numerical dispersion relations for the local Cartesian SWEs to analyze their influence on the characteristic waves of the shallow water problem. Our main focus was on the advective wave, which is most important in meteorological applications. For characteristic step sizes, both methods did not significantly affect the advective wave phase velocities. Their influence on the gravity waves, however, was very different. Ros3 with AMF damped these waves more rigorously than Strang splitting, but better represented their phase velocities. In addition, Strang splitting could lead to amplification of these waves, which makes it unsuitable for long time integration periods. Third, we applied both methods to Test 2, Test 5 and Test 6 of the SWEs test set. The numerical results agreed with the theoretical results with respect to the local error and the numerical dispersion relations. Furthermore, they showed that Ros3 with AMF is unaffected by the chosen splitting and, most important, Ros3 with AMF is far more efficient than Strang splitting.

In conclusion, Ros3 with AMF makes a good candidate to efficiently solve the semi-discrete SWEs on a global fine resolution lat-lon grid. Strang splitting, on the other hand, is inadequate in view of its inefficiency and large local error in the polar area.

Acknowledgment

The investigations were in part supported by the Research Council for Earth and Lifesciences (ALW) with financial aid from the Netherlands Organization for Scientific Research (NWO). Project Nr. 750.197.12.

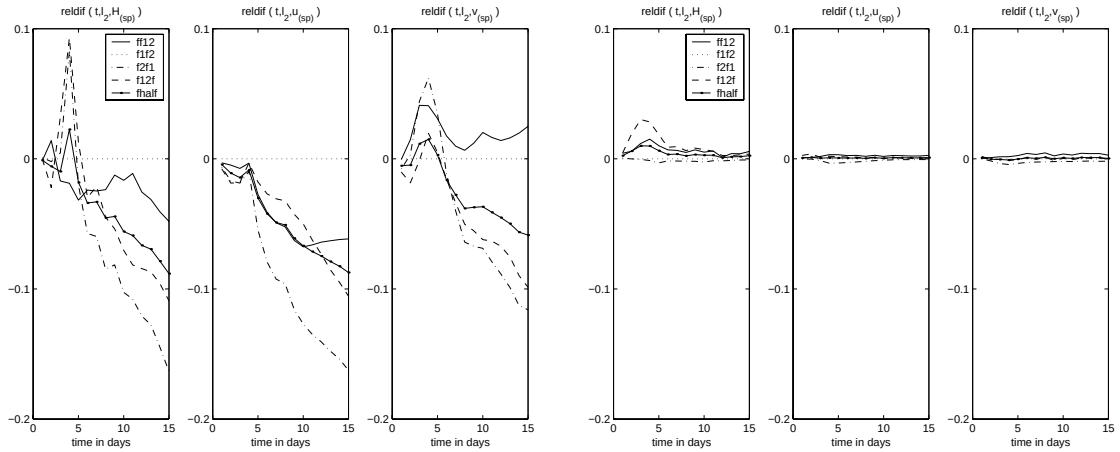

(a) Strang splitting ($\tau = 900$ s) (b) Ros3 with AMF ($\tau = 1800$ s)

Figure 6: The relative differences, reldif(t, l_2, H), reldif(t, l_2, u) and reldif(t, l_2, v), in case of Test 5 for the splittings (ff12), (f1f2) etc. Splitting (f1f2) is used as the reference splitting. Results are presented for Strang splitting (fig(a)) and Ros3 with AMF (fig(b)).

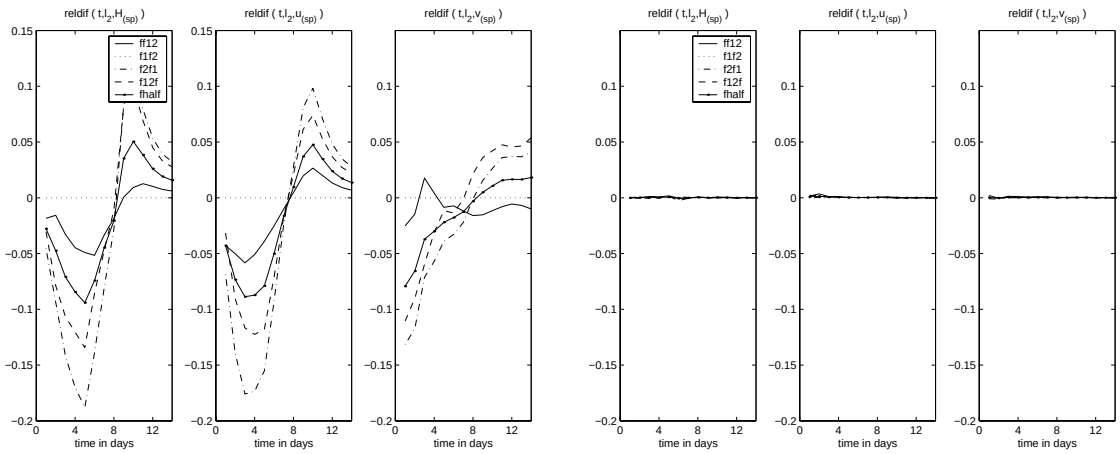

(a) Strang splitting ($\tau = 150$ s) (b) Ros3 with AMF ($\tau = 450$ s)

Figure 7: The relative differences, reldif(t, l_2, H), reldif(t, l_2, u) and reldif(t, l_2, v), in case of Test 6 for the splittings (ff12), (f1f2) etc. Splitting (f1f2) is used as the reference splitting. Results are presented for Strang splitting (fig(a)) and Ros3 with AMF (fig(b)).

References

1. R.M. Beam and R.F. Warming. An implicit finite-difference algorithm for hyperbolic systems in conservation-law form. *J. Comput. Phys*, 22:87–110, 1976.
2. R.A. Brown. *Fluid mechanics of the atmosphere.* Academic Press, San Diego, 1991.
3. K. Dekker and J.G. Verwer. *Stability of Runge-Kutta methods for stiff nonlinear differential equations.* North-Holland, 1984.
4. E.G. D'yakonov. Difference systems of second order accuracy with a divided operator for parabolic equations without mixed derivatives. *USSR Comput. Math. Math. Phys.*, 4(5):206–216, 1964.
5. B. Gustafsson, H-O. Kreiss, and J. Oliger. *Time dependent problems and difference methods.* John Wiley & Sons, Inc., New York, 1995.
6. E. Hairer and G. Wanner. *Solving Ordinary Differential Equations II. Stiff and Differential-Algebraic Problems.* Springer-Verlag, Berlin, 2nd edition, 1996.
7. G.J. Haltiner and R.T. Williams. *Numerical Prediction and Dynamic Meteorology.* Wiley, 2nd edition, 1980.
8. J.R. Holton. *An introduction to dynamic meteorology.* Academic Press, San Diego, 3rd edition, 1992.
9. P.J. van der Houwen and B.P. Sommeijer. Approximate factorization for time-dependent partial differential equations. *J. Comput. Appl. Math.*, 128:447–466, 2001.
10. D. Lanser, J.G. Blom, and J.G. Verwer. Spatial discretization of the shallow water equations in spherical geometry. *J. Comput. Phys.*, 165(2):542–565, 2000.
11. D. Lanser, J.G. Blom, and J.G. Verwer. Time integration of the shallow water equations in spherical geometry. *J. Comput. Phys.*, 171:1–21, 2001.
12. D. Lanser and J.G. Verwer. Analysis of operator splitting for advection-diffusion-reaction problems from air pollution modelling. *J. Comp. Appl. Math.*, 111:201–216, 1999.
13. D.W. Peaceman and H.H. Rachford Jr. The numerical solution of parabolic and elliptic differential equations. *J. Soc. Indust. Appl. Math.*, 3:28–41, 1955.
14. J. Pedlosky. *Geophysical Fluid Dynamics.* Springer-Verlag, New York, 2nd edition, 1987.
15. J.M. Sanz-Serna. Geometric integration. In I.S. Duff and G.A. Watson (Eds.), editors, *The State of the Art in Numerical Analysis*, pages 121–143. Clarendon Press, Oxford, 1997.
16. J.M. Sanz-Serna and M.P. Calvo. *Numerical Hamiltoninan Problems.* Chapman and Hall,

1994.

17. G. Strang. On the construction and comparison of difference schemes. *SIAM J. Numer. Anal.*, 5:506–517, 1968.
18. P. Wesseling. *Principles of computational fluid dynamics*, volume 29 of *Springer Series in Computational Mathematics*. Springer-Verlag, Berlin, 2001.
19. D.L. Williamson. Review of numerical approaches for modelling global transport. In H. van Dop and G. Kallos, editors, *Air Pollution modelling and its Application IX*, New York, 1992. Plenum Press.
20. D.L. Williamson, J.B. Drake, J.J. Hack, R. Jacob, and P.N. Swarztrauber. A standard test set for numerical approximations to the shallow water equations in spherical geometry. *J. Comp. Phys.*, 102:211–224, 1992.